



Universiteit
Leiden
The Netherlands

Chasing cosmic tau neutrinos in the abyss

Bormuth, R.; Bormuth R.

Citation

Bormuth, R. (2017, December 7). *Chasing cosmic tau neutrinos in the abyss*. *Casimir PhD Series*. Retrieved from <https://hdl.handle.net/1887/56023>

Version: Not Applicable (or Unknown)

License: [Licence agreement concerning inclusion of doctoral thesis in the Institutional Repository of the University of Leiden](#)

Downloaded from: <https://hdl.handle.net/1887/56023>

Note: To cite this publication please use the final published version (if applicable).

Cover Page



Universiteit Leiden



The handle <http://hdl.handle.net/1887/56023> holds various files of this Leiden University dissertation.

Author: Bormuth, R.

Title: Chasing cosmic tau neutrinos in the abyss

Issue Date: 2017-12-07

DETECTION UNIT PROTOTYPE

The future can ever promise but
one thing and one thing only:
surprises

Steven Erikson, House of Chains

4.1 INTRODUCTION

The preproduction model of a detection unit (PPM-DU) is a small scale string prototype made of 3 digital optical modules (DOMs). It was installed in May 2014 just 80 km off the Sicilian coast at a depth of 3500 m. The deployment was performed using a launcher optical module (LOM [97]), the procedure being equivalent to a final configured string. The total data taking period lasted from May 2014 to July 2015 with longer pauses inbetween due to maintenance or improvements on the deep sea infrastructure. Together with the previously deployed (April 2013) DOM prototype (PPM-DOM [98], for more details see below) at the ANTARES site in France the PPM-DU is the first DOM and string prototype installed by the KM₃NeT collaboration. A picture of the three DOMs of the PPM-DU installed on the launcher module is shown in Fig. 19.

The expected observations for the prototype are potassium decays, bioluminescence events and atmospheric muon events. Due to the small instrumented volume and statistics discussed below neutrino observations are not expected. In addition, the distinction between muon and neutrino signals is not possible due to the large probability of misreconstructed track parameters.

In this chapter the technical design, data taking methods, detector calibration and data analysis of the data from the PPM-DU will be discussed.

The DOM prototype

The first DOM prototype was deployed at the ANTARES site in April in 2013. It was installed on the ANTARES instrumentation line (IL [66]) at a depth of 2375 m about 100 m above the sea floor. The IL provides the PPM-DOM with the power supply and read-out to shore, making the PPM-DOM an autonomous detector within the ANTARES observatory. In Fig. 23 the PPM-DOM is shown attached to the instrumentation line with an ANTARES holding structure. The PPM-DOM holds ETEL PMTs of the type D783KFLA [99] as described in Sec. 4.2.

Operation covered about one year. In total 41.5 hours of data, which are feasible for analysis, have been recorded. The PPM-DOM analysis established



Figure 23: The PPM-DOM attached to the ANTARES instrumentation line before deployment.

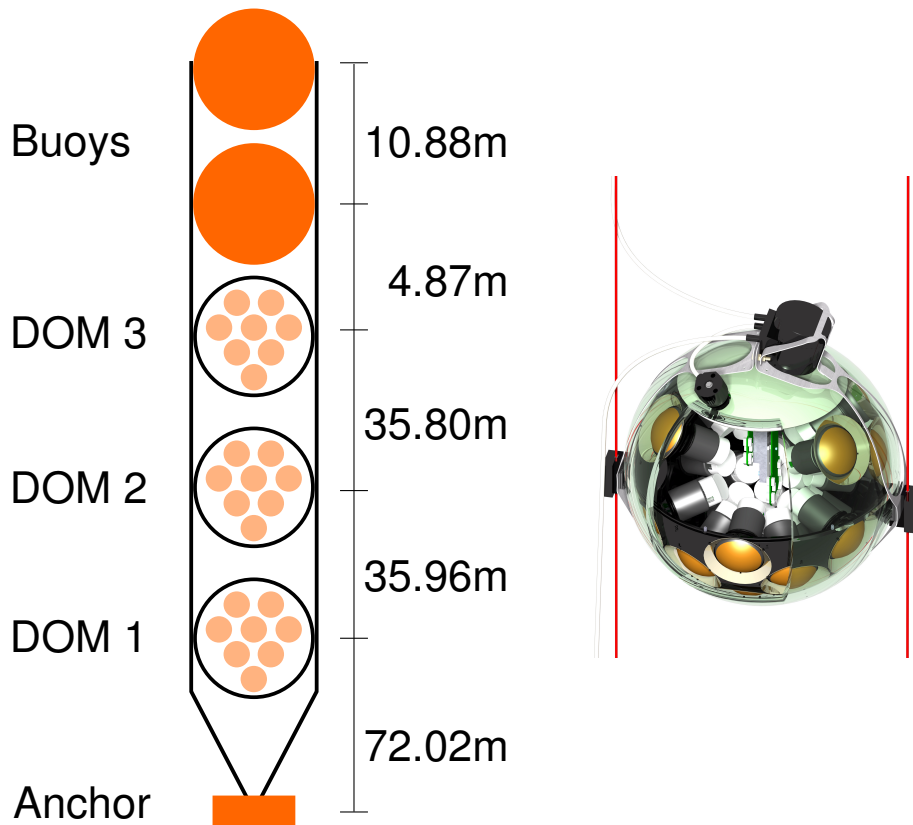
the PMT time calibration by observing potassium decays. Together with the PMT calibration the analysis of the PMT properties such as the single rate and angular dependence of coincident light allowed for a characterization of the small PMTs in the deep sea. The first observations of muons based on a single DOM with the multi-PMT design have been accomplished.

4.2 TECHNICAL DESIGN

The PPM-DU is a shortened string of a total length of about 160 m. It is attached to the ground via an anchor structure and holds three DOMs and two empty glass spheres is shown in Fig. 24a. On the anchor platform a base module [100] is situated. The base module functions as an interface between the detection unit and the sea floor network. The string is held upright by the buoyancy of the DOMs and the empty glass spheres.

Each DOM holds 31 PMTs, the corresponding read-out electronics, power supply as well as other supplementary sensors and devices. The supplementary installations include a LED light source (nano beacon [86]), an acoustic sensor [85], a compass and a tilt meter for time, position and orientation calibration, respectively.

The DOMs attached to the string differ from standard KM₃NeT DOMs. The main differences are the central logic boards (CLBs), compass and PMTs. A technical drawing of a DOM and many components it holds is shown in Fig. 24b.



(a) A sketch of the PPM-DU; DOM 1 and 2 contain ETEL PMTs while DOM 3 contains Hamamatsu PMTs. (b) A sketch of a DOM attached to a string.

Figure 24: Sketches of the PPM-DU and the DOMs.

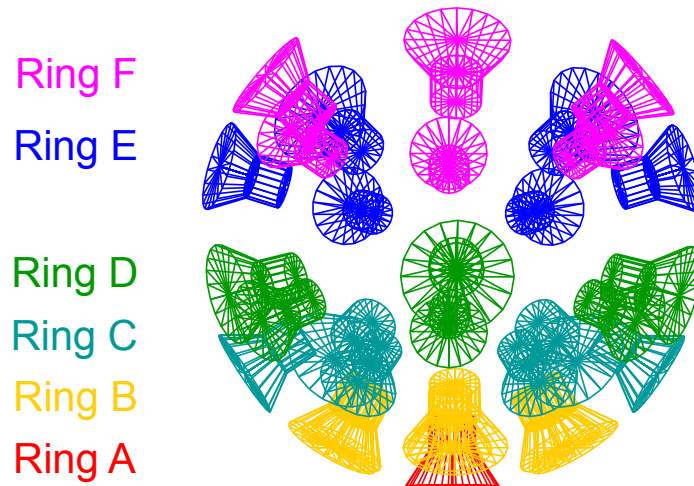


Figure 25: Sketch of the PMTs within a DOM; color indicates the ring; within the rings the PMTs are numbered from 1 to 6 depending on their zenith and phi angle.

The CLBs are prototype productions and hence lack some functionality. Among the missing features are the absence of a functioning positioning system and the loss of timing information on the installed LEDs.

The compass inside the PPM-DU DOMs is non functional. A measurement of the orientation of the DOMs was therefore not possible.

The PMTs are numbered and named according to their position in ring and angle is shown in Fig. 25 (see also Tab.4). The three DOMs have different installed PMT types. In DOM 1 and DOM 2 PMTs of the manufacturer ETEL of the type D783KFLA [99] are installed. DOM 3 holds PMTs produced by Hamamatsu of the type R12199-02 [83]. The main difference between the PMTs is the diameter of the photo-cathode area of 77 mm (ETEL) and 80 mm (Hamamatsu), respectively. Each PMT inside the DOM is surrounded by a reflecting aluminum ring at an angle of about 45° [82]. The reflector rings have a width of 17 mm (ETEL) and 18 mm (Hamamatsu).

Each PMT has its own power supply and electronics called PMT base [84]. The base is attached to each dynode and cathode of a PMT and provides them with the necessary high voltages. In addition, it converts the analog signal into a digital signal by a time over threshold method. For this, a threshold value equivalent to 30% of the charge produced by a single photo electron is used. The time the signal is above the threshold is then passed on to the CLB. The so produced digital signal is referred to as the time over threshold signal (ToT).

The PMTs are operated at an amplification of about 5×10^6 which yields an average ToT of about 30 ns for a single photo electron. The discrimination and digitization of the analog signal are performed by custom ASICs on the PMT base. The recorded ToT is limited to a maximum value of 256 ns. A signal extending beyond this value will be split in separate data. The original signal can be recovered by combining these data.

4.3 DATA ACQUISITION SYSTEM

The PPM-DU data acquisition system (DAQ) transfers the complete detector data to shore. The raw data packages are organized in segments called time slices of 134 ms duration. Each time slice contains a frame per DOM in which the hit information (hit time and ToT) of that DOM is stored. The hit time is determined relative to the internal clock of every DOM. The clock and data transfer per DOM is managed within the CLBs.

On shore the data is further processed by applying selection criteria to minimize the amount of background events recorded, this process is called triggering (see Sec. 4.3.1). During nominal data taking a total of 24 runs of 30 min length are recorded per day. The length of a run is limited by the file size of the raw data files. During the night these runs are processed with the standard trigger and the processed data is copied to the computing center. Per day one raw data file is recorded for minimum bias studies. This corresponds to a total data taking of 18 h. The fact that simultaneous data taking and triggering are not possible is caused by the prototype nature of the PPM-DU and the corresponding on shore facilities.

4.3.1 Trigger algorithm

The applied trigger algorithm selects from the raw data streams triggered events based on time correlations of the recorded hits. In order to be able to make statements about timing correlations the data is time calibrated (for more information on the time calibration see Sec. 4.5). After applying the time calibration the trigger algorithm scans raw hits (Lo) on the same DOM with a time difference smaller than 25 ns. Such a pair of hits is called L1 hit. The time of a L1 hit pair is set to the time of the earlier hit that constitutes the L1 hit. Once at least one L1 hit on a DOM is found a so called triggered event is recorded. A triggered event contains all Lo hits that form a L1 hit within a time window as given in Eq. 16 after the first recorded L1 hit.

$$t_{\text{first L1}} - t_{\text{last L1}} = \text{dst}(\text{DOM}_1, \text{DOM}_3) / c_{\text{water}} + T_{\text{extra}} (\equiv 20 \text{ ns}) \approx 330 \text{ ns} \quad , \quad (16)$$

where $\text{dst}(\text{DOM}_1, \text{DOM}_3)$ is the distance between top and bottom DOM and c_{water} is the speed of light in water for an average refraction index of $n \approx 1.38$. The time window corresponds to the maximum travel time difference between unscattered light emitted from a point. In addition to the Lo hits forming a L1 all Lo hits are stored in an extra ± 20 ns around the triggered event. All Lo hits within 20 ns on one DOM form a so called coincidence. The size of a coincidence corresponds to the number of hits that constitute it.

The parameters that govern the trigger behavior that are tunable are therefore the used distance $\text{dst}(\text{DOM}_1, \text{DOM}_3)$, the additional time T_{extra} , number of triggered L1 hits and the L1 hit time window. The used values in the PPM-DU trigger are chosen in order to record as much data as possible, since with only three DOMs the data size is small enough to allow for this approach. With

more strings and DOMs in the future KM₃NeT detector the trigger parameters need to be more restrictive to cope with the large amount of data produced by the detector.

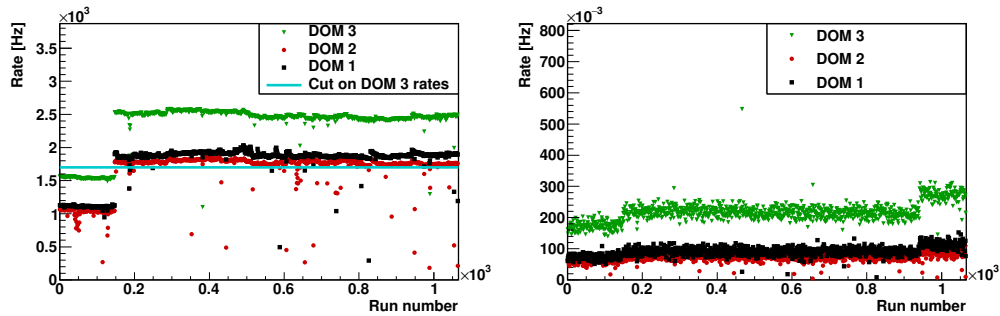
The triggered events, together with time slices of all L1 hits and some auxiliary information (PMT rates) are stored in a ROOT formatted file [101]. A triggered ROOT file contains three main branches: the triggered event, the L1 time slices and the summary slices. The L1 time slices are all L1 hits time sorted within a run and the summary slices contain the rates of each PMT per slice.

4.3.2 Recorded data

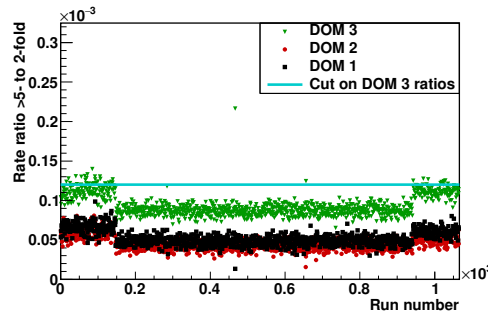
The data taking of the PPM-DU can be separated into three distinct periods by long breaks in data taking and changes in detector operation. The exact duration and data available in the different periods are summarized in Tab. 1. The first period differs most noticeably from the others due to manual data recording and early data taking variations (single DOM runs, problematic PMTs and different trigger setups) which causes a small amount of usable data. The second and third phase both have automatic data taking and a small amount of special runs. Period two and three are distinguished by a long break in data taking of 6 weeks and the use different of software versions for triggering.

The total amount of recorded data does not necessarily correspond to the amount of data available for data analysis. Runs are only suitable for general data analysis if they fulfill a range of criteria. The quality criteria are linked to the detector performance and detector operation mode.

The detector performance requirements are based on the rates of different coincidence sizes during data taking. Shown in Fig 26 are the rates as a function of coincidence size and the ratios between coincidences of different size. For the rates we observe shown in Fig. 26a groups of runs for which the 2-fold rate drops by a significant margin from the baseline for all three DOMs simultaneously. The cause for this drop is not identified, but could be linked to data transfer issues. In order to remove these runs from standard data analysis all runs in which DOM 3 has a 2-fold rate ≤ 1200 Hz are excluded. In addition to the drop in rates a scatter from the baseline for high coincidence sizes is visible as shown in Fig. 26b. Since the scatter could correspond to a variation in the singles rates indicating non-optimal data taking conditions we cut on the ratio between the 2-fold and rate and the 6-fold or higher rates of $>5\text{-fold}/2\text{-fold} \leq 0.12 \times 10^{-3}$ as shown in Fig. 26c. All three Figures shown in Fig. 26 show steps in the respective rates at the same time. The first step around run number 180 is related to a major upgrade in the triggering software. The update was needed after the triggering of the early runs in phase 2 was found defective for yet unknown reasons. The early runs were retriggered with the new software, but some defective effects remained. The second step to higher rates for coincidence sizes larger 2 at around run number 950 is also correlated with a change in the trigger algorithms. The cluster algorithm was updated, triggering more coincidences of higher size.



(a) Rate of 2-fold coincidences and cut value (see text). (b) Added rates of 6-fold and higher coincidences.



(c) Rate ratios of the added 6-fold and higher coincidences to 2-fold and cut value (see text).

Figure 26: Quality plots for the runs of phase 2 based on rate information.

The detector operation mode used for runs which enter the standard analysis is three DOMs taking data operating all functional PMTs at nominal HV. This data taking mode is considered standard operation mode and is the most frequent way the detector is operated. There are two PMTs which are non functional and turned off during standard operations (DOM 2: B1 and DOM 3: D5). PMT B1 in DOM 2 was not addressable since deployment while PMT D5 in DOM 3 was functional at first. But, after 3 months of operation, rates above 300 kHz have been observed and it was turned off since.

Other detector operation modes are excluded from this analysis. These modes include the flashing of the LED nano beacons, single DOM data runs and operating PMTs at non-nominal voltages.

Table 1: Summary of the data taking periods of the PPM-DU.

	first run taken	last run taken	usable data [h]
phase 1	07-05-2014	03-08-2014	65 h ^a
phase 2	25-08-2014	15-12-2014	456 h ^b
phase 3	22-01-2015	09-07-2015	565 h ^c

a data quality analyzed

b see footnote a

c total recorded runtime

4.4 PPM-DU MONTE CARLO SIMULATION

Monte Carlo simulations (MC) are an essential tool to understand, quantify and verify the collected data. By comparing distributions between data and MC inconsistencies can be identified.

Two kind of simulations have been performed for the PPM-DU. One contains atmospheric muon events with an added potassium background and the other a small sample contains of potassium background only.

The muon MC production simulates the expected signals from muons which are produced in the atmosphere by air showers. These are caused by high energetic cosmic rays impinging on Earth's atmosphere. The interaction with atoms in the atmosphere cause a cascade of energetic particles. Among these are muons which at relativistic energies have a lifetime long enough to reach the detector at the sea floor. The number of expected muons at a given sea level and data taking duration is determined using the MUPAGE code [102]. For this purpose the complex simulations of full air showers are substituted by a set of simple formulas [103]. The number of expected muons per shower (muon multiplicity) is taken from a complete air shower simulation. For the purpose of the PPM-DU simulations muons with energies of $E_{\mu} \geq 10$ GeV and a zenith angle range of 0° to 85° are produced. An equivalent of 15.3 d of statistics have been simulated.

The MUPAGE code only generates muon tracks in a certain volume around the detector and calculates the corresponding lifetime of the MC file. If a muon track reaches a certain area around the DU (the can) its light production is simulated using the KM3 program [104]. The considered light production mechanisms are cherenkov light and Bremsstrahlung (causing showers). The light production is simulated using look up tables produced by a designated application based on GEANT for fast processing. The light is then propagated through the water, taking into account the processes of light scattering and absorption in the sea water. In this, the measured water properties of the PPM-DU site have been used [105]. The simulation also takes into account the interaction of the light with the glass spheres of the DOMs. the reflector rings and the angular acceptance of the PMT cathodes.

The response of the detection unit including hit time smearing caused by the PMT transit time and converting photo electrons to ToT signals is simulated

using JPP software package [96]. The determined PMT efficiencies (see Sec. 4.5.1) are taken into account when simulating the response of a PMT to an incident photon. Depending on the efficiency of each PMT the corresponding percentage of the incident photo electrons are discarded. To counteract limitations caused by this rejection, the complete light production is scaled up by a factor 1.1.

The pure potassium MC is based on the single rates recorded with the PMTs. From the observation of the single rates the corresponding expected rates for observing coincidences of size 2, 3 and 4 have been calculated using a designated GEANT 4 simulation. For the single rates a rate of 5.5 kHz was assumed corresponding to correlated rate of 697 Hz (size 2), 57 Hz (size 3) and 7 Hz (size 4). The expected number of potassium hits is added to the muon MC.

In order to have a pure background sample which can be matched to data a dedicated potassium MC is created which consists of time slices filled with potassium hits only.

4.5 IN-SITU DETECTOR CALIBRATION

In this section, the possibilities of in-situ time calibration methods for a string like detection unit are presented, which are discussed in more detail in a KM₃NeT internal note [106]. The main task of the in-situ calibration is an exact understanding of the detector properties in a fully assembled state. The PMT characterization in the lab does not include the time calibration of all 31 PMTs in a DOM (intra DOM time calibration) in an assembled state. Many parameters established pre-deployment could be influenced by the surrounding conditions such as temperature or stress during deployment and therefore need to be re-established. The DOM time calibration (inter DOM time calibration) needs to be determined since it was lacking. Especially the time calibration is essential for any measurement performed with the detector. The trigger and reconstruction algorithms are based on timing information with a precision at the ns level. The time calibration of the detector has to achieve a precision of the order of ns or ideally sub-ns to allow for an optimal performance of the algorithms. Just as important as the precision is the long term stability and monitoring of the time calibration. The time offsets are stored in a data base for later use during data analysis. In addition to the time offsets other properties of the PMTs need an in-situ calibration method. These are discussed in detail in Sec. 4.5.1.

The prototype nature of the PPM-DU has an impact on the time calibration for two reasons: The lack of a functional pre-deployment time calibration and the lack of a white rabbit system on the CLBs.

The white rabbit system guarantees that after a reboot of the detector each DOM clock is synchronized with the rest of the detector timing system. The exact knowledge of the DOM clocks is crucial since the time of hits are determined with respect to that clock. The consequences of the absence of the white rabbit system will be discussed in the inter DOM time calibration section.

The lack of a pre-deployment calibration makes an in-situ calibration crucial. In addition, the lack of starting parameters causes the in-situ calibration execution difficult. That being the case, the best guess for inter DOM time offsets is based on the light travel time and the estimated lengths of the read-out cables.

Due to the absence of a white rabbit system and a pre-deployment calibrations a muon reconstruction is only feasible after inter and intra DOM time calibration have been established using in-situ methods.

4.5.1 PMT calibration

The PMT calibration procedure was developed within the JPP software package [96]. In this section, the method and results are presented. The PMT characteristics that can be in-situ calibrated are the PMT transit time (corresponds to time offset), the relative detection efficiency and the transit time spread.

The PMT transit time denotes the time it takes for a signal to travel from the cathode to the PMT base read-out. The transit time therefore corresponds to the time offset of each PMT since variations in read-out hardware are negligible. Variations in the transit time between PMTs are caused by internal production differences and are typically in the order of 10 ns.

The relative detection efficiency of the PMT system denotes the likeliness of a PMT detecting an impinging photon relative to a standard PMT. The detection efficiency is a composition of different causes such as the PMT cathode coating, the reflector rings or the homogeneity of the gel in front of the PMTs. It can change as a result of the tuning of the supplied voltage or aging. Exact knowledge of the total detection efficiency is needed in order to allow for precise data to MC comparisons.

The PMT calibration is based on the observation of light from radioactive decays. These decays originate from the natural abundant potassium isotopes (^{40}K) in the sea salt and cause a single rate per PMT of around 5.5 kHz. Since the ^{40}K isotopes decay mainly (89 %) via β decay at an energy of 1.3 MeV the subsequent light production is small. The other decay mode is via electron capture, emitting a γ ray of 1.46 MeV with comparable light production to the β decay. Due to the small light yield correlated observations are limited to a short distance. For a pair of PMTs the observed correlated ^{40}K rate depends on the detection efficiencies of the PMTs and the relative angular distance of the pair. Figure 27c shows the distribution of hit time differences (ΔT) for one PMT pair. The distribution shows an approximately Gaussian peak on top of a constant background. The peak corresponds to the observation of correlated light from ^{40}K decays. Its mean is offset from zero due to the time offsets of the two PMTs forming the pair. The constant background is caused by uncorrelated photons. The hit time difference distribution for all possible combination of PMT pairs on a DOM is shown in Fig. 27a, where the pair ID increases with lower angular distance (pair ID 0 has the largest possible angular distance, pair ID 465 lowest possible angular distance). For each DOM a total of 465 independent combinations between PMTs are possible, with $N_{\text{combinations}} = N(N - 1)/2$ with

$N = 31$ PMTs. Since the observation of correlated ^{40}K signals depends on the angular distance between PMTs, a steady increase in peak area is shown in Fig. 27a.

A χ^2 minimization procedure is applied simultaneously to all distributions evaluating the PMT properties of all PMTs in a DOM. The constant background is subtracted and a Gaussian fitted to each PMT pair distribution. The constant background due to random coincidences is estimated using the recorded PMT rates. The mean values, heights and widths of the Gaussian peaks are related to the time offsets, efficiencies and intrinsic transit time-spreads of the PMTs. In order to translate the area of the Gaussian to a PMT efficiencies a model for the decrease of the coincidence rates due to ^{40}K depending on the angular distance between the PMT pair is assumed (See Eq. 17). A graphical representation of the function (PMT angles on DOM from 33° to 165°) is shown in Fig. 28, the region of interest is indicated by the blue lines.

$$^{40}\text{K}_{\text{rate}}(\theta) = \exp(p1 + \cos(\theta) * (p2 + \cos(\theta) * (p3 + \cos(\theta) * p4)))[\text{Hz}] \quad , \quad (17)$$

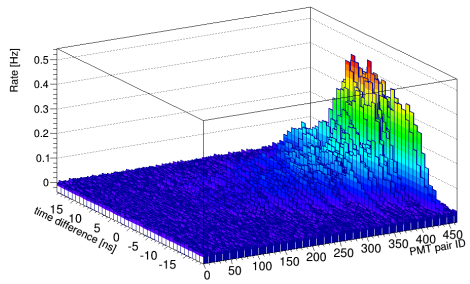
where $\cos(\theta)$ is the angle between the corresponding PMT pair and $p1$, $p2$, $p3$ and $p4$ are taken from a dedicated ^{40}K simulation [107] (for the used values see Appendix Tab. 5).

The results of the PMT calibration for the estimated time offsets, time spread and efficiency are shown in Fig. 29. Here a set of 320 quasi consecutively taken runs at the start of phase 3 data taking have been analyzed (from run number 1544 to run number 1900). A small sub sample of runs have been excluded because a nano beacon was flashing.

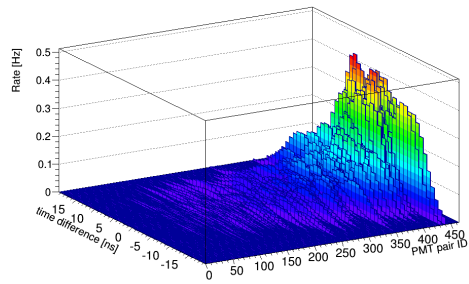
The results for the time offsets shown in Fig. 29a indicate the PMT time offsets to be in the order of ± 10 ns. The obtained calibration values are shifted such that the total offset value is as small as possible. The time spreads shown in Fig. 29b are mainly between 2 ns to 2.5 ns which agrees with the measured average time spread value of 2.3 ns in the pre-deployment PMT testing.

The results for the PMT efficiency are given relative to a reference PMT. Hence, the results shown in Fig. 29c show values larger than one. In phase 3 a second PMT in DOM 2 was taken offline, causing the empty bin in efficiency at PMT ID 20. In order to study the determined efficiencies the correlation between the singles rate and efficiency of a PMT is studied [108]. The single rate of and efficiency of a DOM are found to be well correlated. A correlation between the measured PMT quantum efficiencies pre-deployment and the total efficiency cannot be established as shown in Fig. 30. The lack of a correlation between these is puzzling and at the moment not understood.

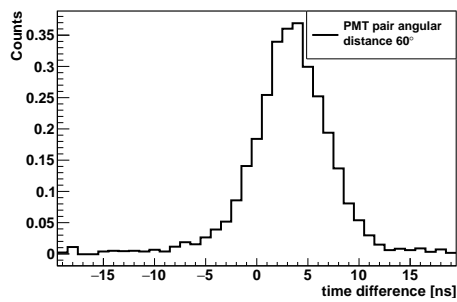
As shown in Fig. 29a and Fig. 29b the parameters of the PMTs in DOM 3 (Hamamatsu) show a lower scatter than the PMTs in DOM 1 and 2 (ETEL). Also for the efficiencies shown in Fig. 29c the results for DOM 3 are different, showing a higher total efficiency. The reason for the higher efficiencies in DOM 3 is expected due to a larger surface of the installed reflector rings and the larger cathode area of the Hamamatsu PMTs. For the stability of the obtained PMT calibration during this time see Sec. 4.5.2.



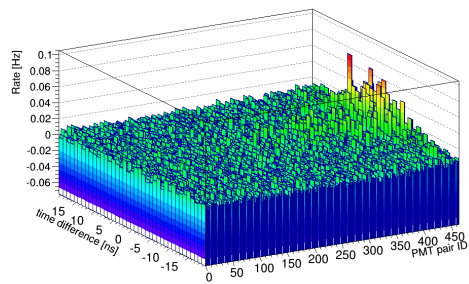
(a) ΔT distributions for all PMT pairs; y-axis sorted by angular distance.



(b) Fit to all ΔT distributions for all PMT pairs; y-axis sorted by angular distance.



(c) ΔT distribution for one PMT pair (channels F1 and F6).



(d) Z-axis shows Fig. 27a - Fig. 27b; y-axis sorted by angular distance.

Figure 27: PMT time calibration performance for DOM 1 in run 1547.

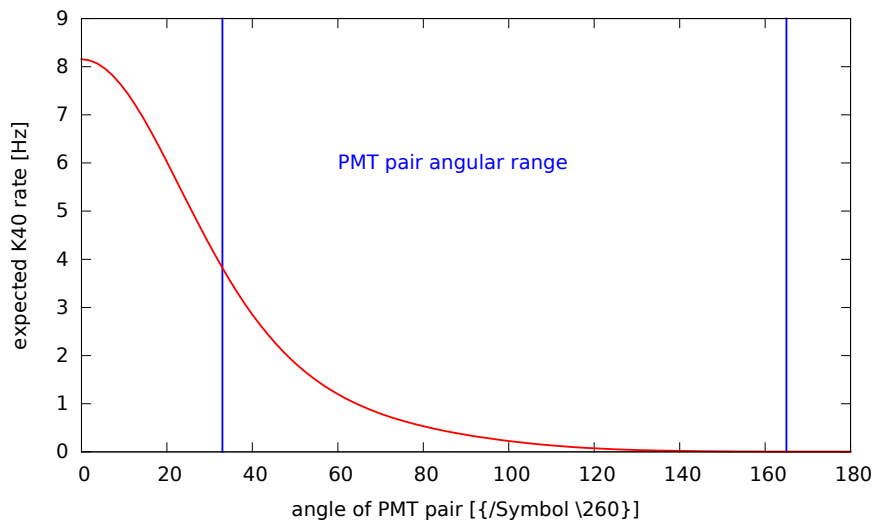


Figure 28: Estimated ^{40}K rates for a certain PMT pair angular distance.

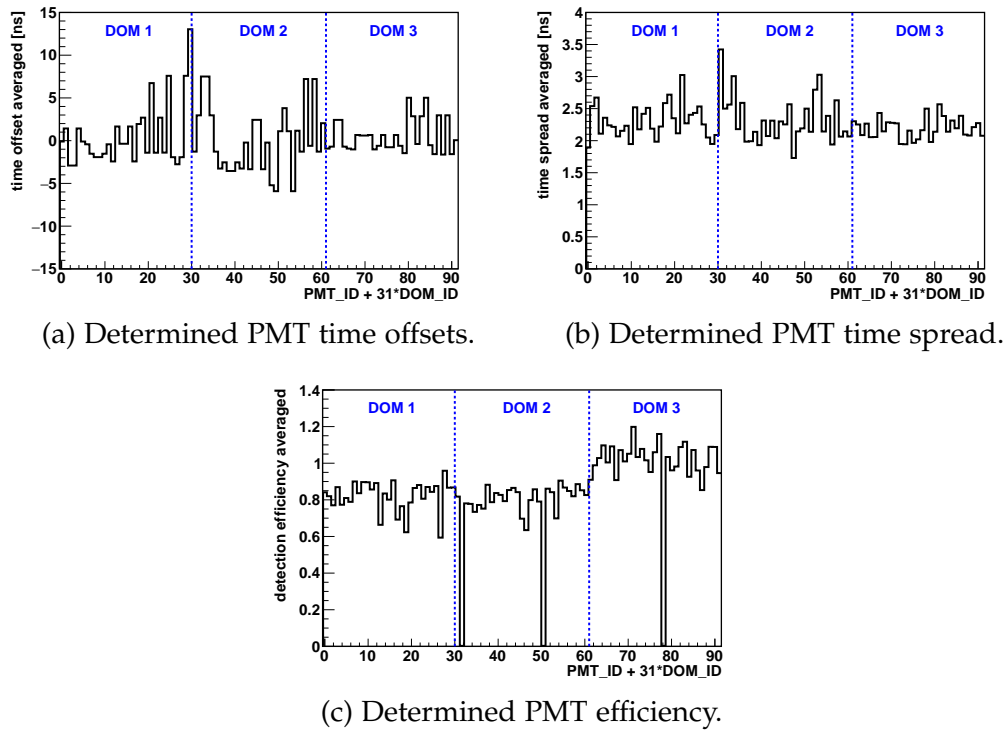


Figure 29: PMT time calibration results for 320 runs taken consecutively at the end of phase 2 and the beginning of phase 3.

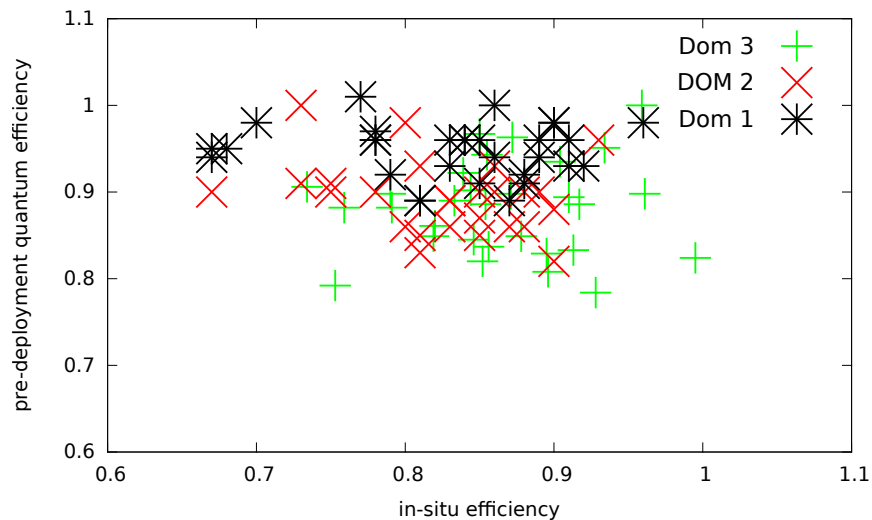


Figure 30: The pre-deployment PMT quantum efficiency plotted against that determined in-situ PMT efficiency; in-situ PMT efficiency value is scaled for a better comparison.

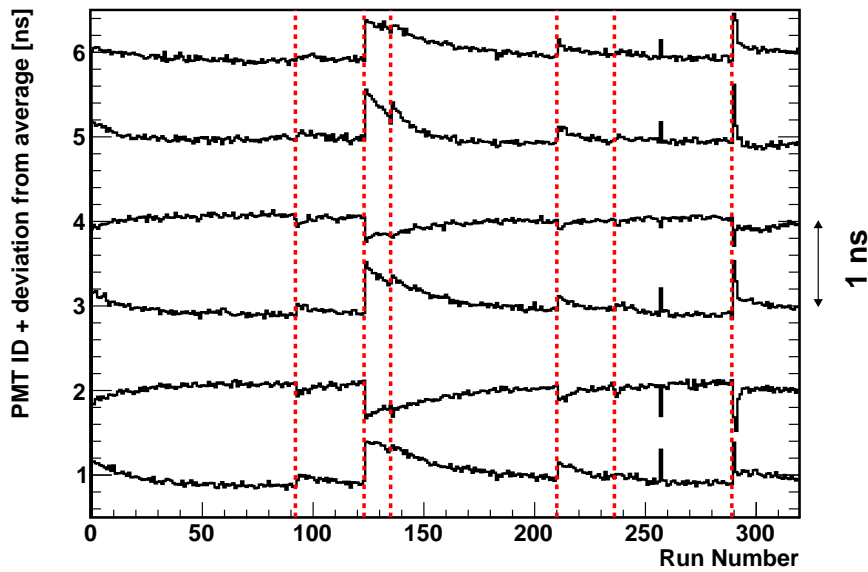


Figure 31: Long term behavior of PMT time offsets for DOM 1 Ring B; y-Axis shows the deviation from the average time offset for the corresponding PMT offset by the PMT ID, the difference in ns between y-Axis for two PMTs corresponds to exactly 1 ns; red lines indicate breaks in the data taking lasting between hours and months; runs taken between December 11, 2014 and July 9, 2015.

4.5.2 PMT calibration stability studies

The study of the long time behavior of the PMT calibration parameters is briefly discussed here and in more detail in [108]. The parameters are monitored for every run taken from December 11, 2014 to July 9, 2015 which includes runs from the end of data taking period 2 and the start of data taking phase 3. The values of parameters have been obtained for every third run. The results on PMT time-offsets, time transition and efficiencies vary and are discussed below.

In order to study the stability of the calibration parameters the deviation of the mean value is plotted over the data taking period for every PMT on each DOM. One such plot for Ring B of DOM 1 is shown in Fig. 31. The calibrated PMT time offsets are stable within the sub nano second range. The PMT time offsets are found to occasionally change up to a nano second and relax back to the original offset within a day. These seemingly spontaneous deviations correlate with breaks in the data taking that lasted between hours and months indicated by the dashed red lines. These changes in time offsets are linked to hardware effects on the PMTs such as temperature change or charge built up.

The PMT time spread calibration parameters behave like the PMT time calibration showing a sub nano second spread and spontaneous deviations up to a nano second correlated with breaks in data taking.

The PMT efficiencies are found to show the largest variations. The efficiencies of the PMTs looking upward (top two rings) are degrading with time and some

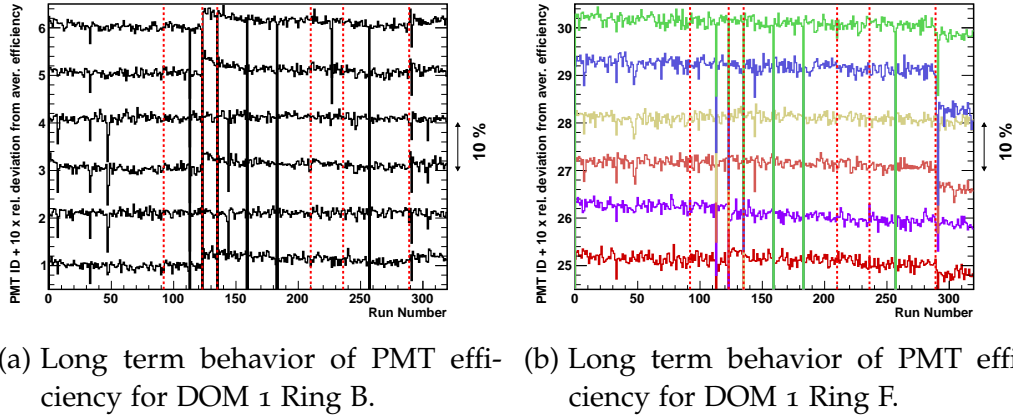


Figure 32: Long term behavior of PMT efficiency for DOM 1; y-Axis shows the relative deviation from the average efficiency for the corresponding PMT offset by the PMT ID, the difference in relative efficiency between y-Axis for two PMTs corresponds to exactly 10%; red lines indicate breaks in the data taking lasting between hours and months; runs taken between December 11, 2014 and July 9, 2015.

PMTs show a spontaneous recovery of the efficiencies. Two histograms showing the relative deviation of the average PMT efficiency for Ring B and F of DOM 2 are shown in Fig. 32.

The degradation in efficiency of the two upper rings can be up to 20% from the original efficiencies as measured at the start of the PPM-DU data taking. The recovery is not correlated to any quantifiable hardware or software changes. The two effects together lead to the conclusion that the top of the DOMs accumulate dust at the glass of the spheres. This assumption is supported by the fact that the lower ring PMTs do not undergo any efficiencies changes. The spontaneous recovery also supports this assumption since it seems to indicate the material can slide off the glass sphere due to movement of the DOMs or the sea current.

The assumption of efficiency losses being linked to material on the glass sphere is further supported by a visual inspection of the PPM-DU during a sea operation. The pictures shown in Fig. 33 clearly show that all three DOMs of the PPM-DU accumulated dust on the top which was not observed right after deployment and could cause the previously discussed decrease in efficiency.

4.5.3 DOM beacon calibration

The nano beacons installed in every DOM are a flashable LED light source that allows for an inter DOM time calibration [86]. They are positioned between PMTs F3 and F4 in the PMT support structure pointing upwards. The beacons emit light at a wavelength of 470 nm with variable frequency and intensity. The frequency can be varied between 250 Hz to 8192 Hz and the intensity is controlled by the supply voltage which can be varied between 0 V to 24 V. A calibration for the intensity of the light flux is not known, therefore the



(a) DOM 1.



(b) DOM 2.



(c) DOM 3.

Figure 33: Pictures taken during sea operation in December 2015 of the DOMs of the PPM-DU showing accumulation of dust at the top of the DOMs.

ideal intensity was calibrated by taking beacon runs at different intensities and measuring the light on the neighboring DOM. The rise time of the light flash is between 5 ns to 10 ns.

The DOMs in the PPM-DU are time calibrated with respect to the lowest DOM (DOM 1). The original method foresaw to calibrate each DOM with the nano beacon on the DOM directly beneath it. Due to a lack of runs in which the beacon of DOM 2 was operated this approach was not feasible. Hence, DOM 2 and 3 are calibrated using runs in which the beacon of DOM 1 is flashing. The difference in time offsets for using beacon 1 (beacon in DOM 1) or beacon 2 (beacon in DOM 2) to calibrate DOM 3 has been studied and is discussed in Sec. 4.5.4.

During the phase 2 and phase 3 data taking no beacon data has been recorded. In order to translate the results from the beacon calibration to these data taking periods an extra calibration has to be performed based on the muon data, see Sec. 4.5.6.

All triggered events with at least one L1 hit (two hits within 25 ns) in DOM 1 and the to be calibrated DOM are used. For every triggered event the time difference between the 2nd hit on each DOM and the assumed light travel time is used. The reason for using the 2nd hit time instead of the 1st is due to the correlation between the nano beacon light profile and the different travel distances between beacon 1 and DOM 2 or DOM 3 (see Sec. 4.5.5). From these time differences the expected travel time of the nano beacon light is subtracted. The travel distance of the light is assumed to be a straight line between beacon and PMT position on the other DOM. The light speed is corrected by the refractive index of the sea water which is measured to be $n_{\text{light}} = 1.39$ for a wavelength of 470 nm (as taken from [109]). The time difference between the DOMs is therefore given by

$$\Delta T_{2/3} = [t(\text{hit}_{2\text{nd}}(\text{DOM}_{2/3})) - t(\text{hit}_{2\text{nd}}(\text{DOM}_1))] - \text{dst}(\text{beacon}, \text{PMT}(\text{DOM}_{2/3})) * (n_{\text{light}}/c)[\text{ns}] \quad , \quad (18)$$

where $t(\text{hit}_{2\text{nd}}(\text{DOM}_{2/3}))$ is the hit time of the 2nd on any DOM and $\text{dst}()$ is the distance between the beacon and the hit PMT on the to be calibrated DOM. The resulting histogram is fitted with a Gaussian function where the mean of the Gaussian denotes the time offset of the DOM. One such histogram for calibrating DOM 2 and DOM 3 using beacon 1 is shown in Fig. 34.

The resulting time offsets for each beacon 1 run in phase 1 are shown in Fig. 35. The DOM 2 offsets show a stable behavior with a variation of around 2 ns while the offsets of DOM 3 are grouped in periods with different mean offsets. Every single period of DOM 3 shows the same stable behavior as for DOM 2. The two changes in mean time offset for DOM 3 coincides with a power outage (first change in mean) of the DU and a repowering of the on-shore system of DOM 3 (second change in mean). These shifts in means are caused by a shift in one of the clocks in the system due to the lack of a reproducible calibration. The repowering of the system can cause the internal clock to come up with a different time offset. The calibration of DOM 3 therefore requires different detector settings for the corresponding periods.

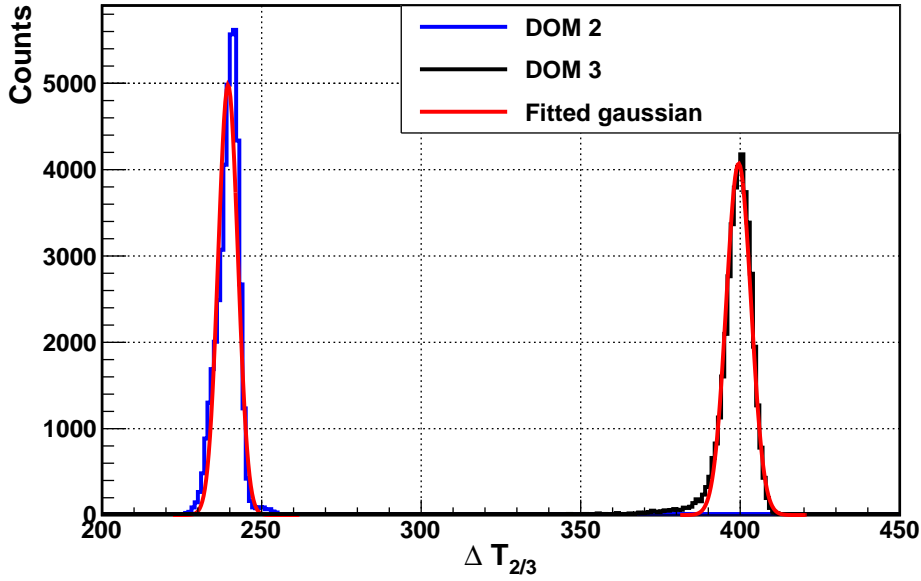


Figure 34: ΔT distributions with Gaussian fit for DOM 2 and DOM 3 relative to DOM 1 with beacon 1 flashing for run 212, DOM 3 data is scaled by the number of entries.

A cross check for the time calibration has been performed by comparing the time differences in the DOMs for muon signals in data and simulation see Sec. 4.5.6 for the results. The time difference distributions in the different DOMs for muon signals are shown in a comparison of data and simulation in Fig. 36 for phase 1 data which have been calibrated according to the nano beacon time offsets. The difference between beacon and muon calibration as determined from these distributions are found to be consistent.

4.5.4 Calibrating DOM 3 using beacon 1 vs using beacon 2

Calibrating DOM 3 with beacon 1 as discussed in Sec.4.5.3 can cause different systematics of the time calibration. Possible effects could be a relatively larger fraction of scattered light due to the larger distance between DOM 3 and beacon 1 or effects connected to the pulse shape of the beacon. In order to check possible changes in the time calibration the results have been compared with those obtained from the available beacon 2 runs (for the results see Appendix Tab. 6). A histogram depicting the fitted time difference distributions for DOM 3 in two runs using beacon 1 or 2 is shown in Fig. 37. One finds that the average time offsets determined from beacon 2 runs is 8.5 ns larger and the fitted σ is 1.9 ns larger than determined by beacon 1 runs (5.2 ns for beacon 1).

The difference in fitted Gaussian σ is attributed to the difference in light travel distance (beacon 2 35.80 m, beacon 1 72.02 m), causing more scattering and absorption of the LED light. The larger time offset cannot be caused by shadowing of DOM 2 one would expect an increased pathway of the light is about 10 cm or so which corresponds to less than 1 ns. A source of the shift in

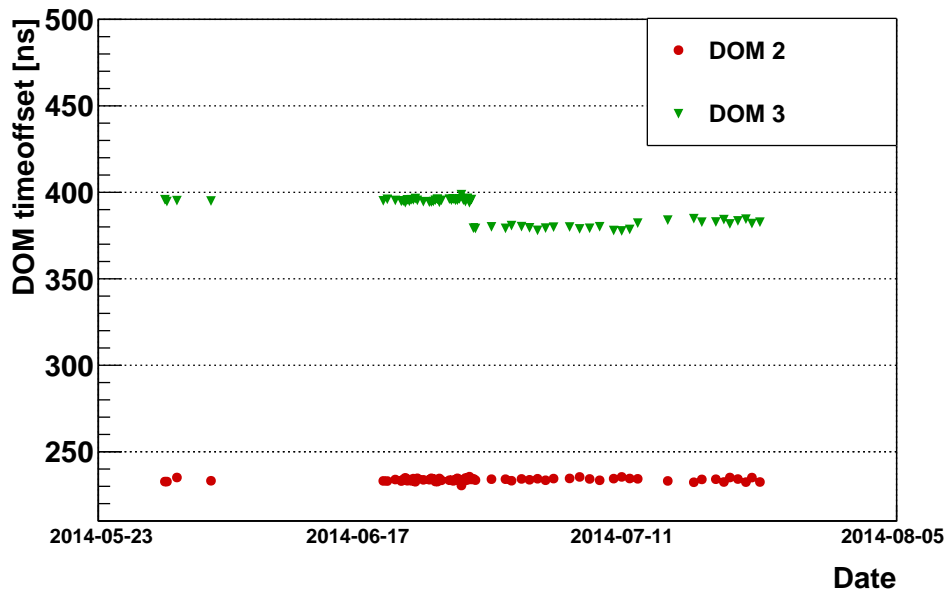


Figure 35: Obtained time offsets for DOM 2 and 3 with beacon 1 in phase 1.

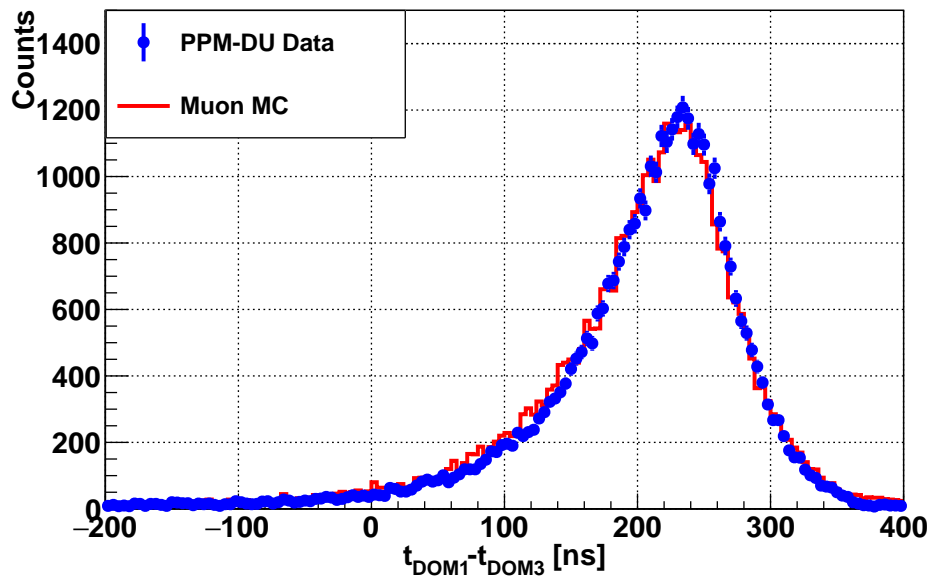


Figure 36: Time difference between DOM 1 and 3 for at least one L1 in every DOM, MC scaled by the number of entries.

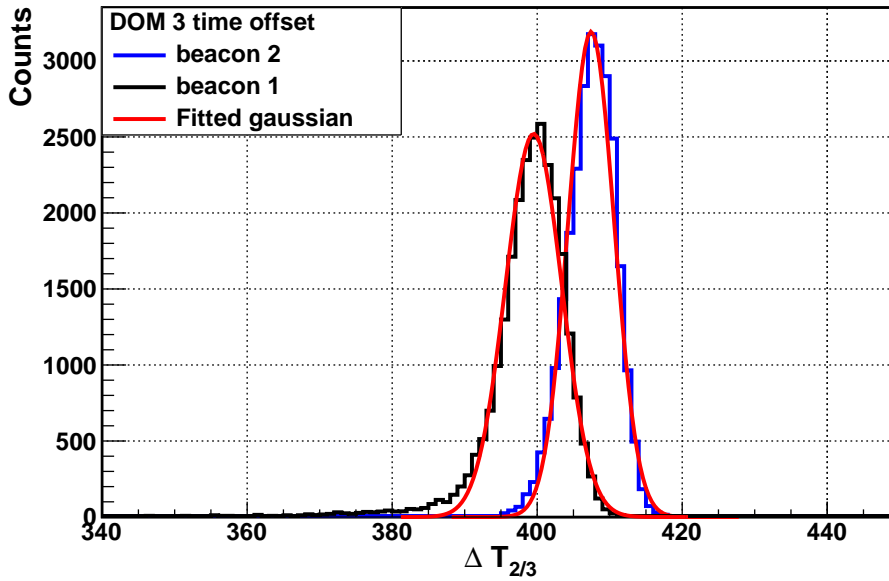


Figure 37: Obtained time offsets for DOM 3 using beacon 1 (run 212) or beacon 2 (run 196); lines show Gaussian fits to the distributions; beacon 1 data scaled by entries.

time offsets could be the rise time of the LED which is around 5 ns to 10 ns. Since DOM 3 is far away from the beacon 1 the arriving light is more likely to be in the main peak of the light burst than in the rising flank. While when the beacon 2 is used to calibrate DOM 3 the distance is much closer and light from the rising flank reaches DOM 3. The determined DOM 3 time offsets with beacon 1 are corrected for this extra offset.

4.5.5 Hit selection: Difference in using 2nd hit vs using 1st hit

A first order approach would suggest to use the time of the 1st hit on a DOM, since the earliest hit is most likely caused by direct light. In the case of the beacon calibration this effect is outdone by effects linked to the nano beacon properties as described below.

The difference between using the first and second hit on the beacon DOM and the to be calibrated DOM (calibrate DOM) has been studied. In the case of using the first hit the ΔT distributions show tails towards early values and the mean of the distribution is shifted to larger time differences (by 5 ns). In order to suppress these tails the effect of using the second hit on the DOMs has been studied. It is found that the distortion of the distribution is mainly caused by the use of the first hit on the DOM. An explanation is that the earliest detected hits are emitted during the rise time of the nano beacon. As shown in Fig. 38a the three DOMs see distinctly different amounts of light from the beacon. The best measure for the number of photo electrons is the recorded ToT, on average a large ToT indicates many incident photo electrons. Looking at the ToT for events recorded during beacon runs shown in Fig. 38b, 38c and 38d we find

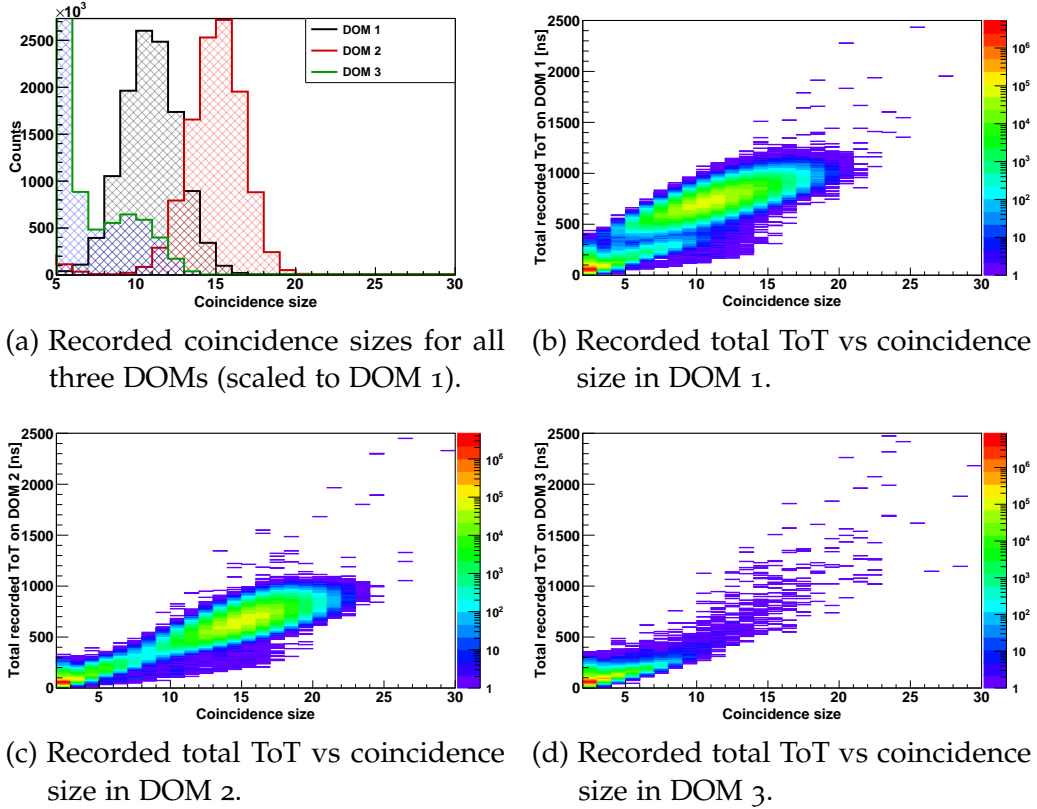


Figure 38: Intensity studies for all beacon 1 runs in phase 1 data taking.

DOM 2 to be the DOM with the largest recorded ToT. Therefore DOM 2 is the DOM which sees the highest light intensity from the beacon. It is more likely for DOM 2 to pick up photons emitted during the rise time of the LED. The effect of using the second hit on the beacon DOM is much more subtle and results in a 1.5 ns shift in the mean of the distribution and reducing the σ from 2.1 ns to 1.8 ns. Due to these findings the second hit was used for the calibration in both DOMs.

4.5.6 DOM muon calibration

As mentioned in Sec. 4.5.3 and shown in Fig. 35 a shift in DOM time offsets has been observed for DOM 3 in data taking phase 1. Such a shift in DOM time offsets is caused the lack of a White Rabbit system as discussed previously. Therefore, any inter DOM time calibration established in phase 1 is not applicable in other data taking phases. During data taking phase 2 no beacon runs have been recorded and therefore a method was devised to translate the DOM time offsets as established from beacon runs in phase 1 to phase 2. The method used for this purpose is based on the observation of muons and will be referred to as the muon calibration [106]. In order for the muon calibration to be performed, the DOM time offsets have to be known with a precision of around 50 ns in order to be able to trigger the muon events. The observed shifts

in the DOM time offsets are of the order of 10 ns to 20 ns and therefore the beacon offsets from phase 1 are a sufficient starting point.

By comparing the time differences for muon signals in the DOMs between data and simulation the DOM time calibration can be validated. The comparison is done using three time difference histograms: Time difference between DOM 1 and 2 (ΔT_{12}), DOM 2 and 3 (ΔT_{23}) and between DOM 1 and 3 (ΔT_{13}). For the first two combinations events with a L1 hit in two DOMs is required and for the last events with a L1 hit per DOM (causing a higher muon purity in this histogram see Chap. 4.6.3). The event selection for the histograms is exclusive (a ΔT_{13} event is not entered in the ΔT_{12} or ΔT_{23} histogram) and the three histograms are therefore independent. In order to reduce the background further a coincidence size selection of events with coincidences ≥ 6 per DOM has been performed which relates to an expected muon rate of about 70 mHz. For each event the time difference between the 1st hit on each DOM pair is filled into the histogram. The histogram for time differences between DOM 1 and 3 is shown in Fig. 36.

The simulation and data histogram for each DOM time difference is then compared with a bin by bin χ^2 method. The resulting χ^2 distributions are fitted with a paraboloid finding the corresponding best matching time offset. The determined time offsets are correlated since $\Delta T_{12} + \Delta T_{23}$ should equal ΔT_{13} . A consistency check is performed and they are found to be within 1 ns agreement. All three established time offsets are then used for the calibration.

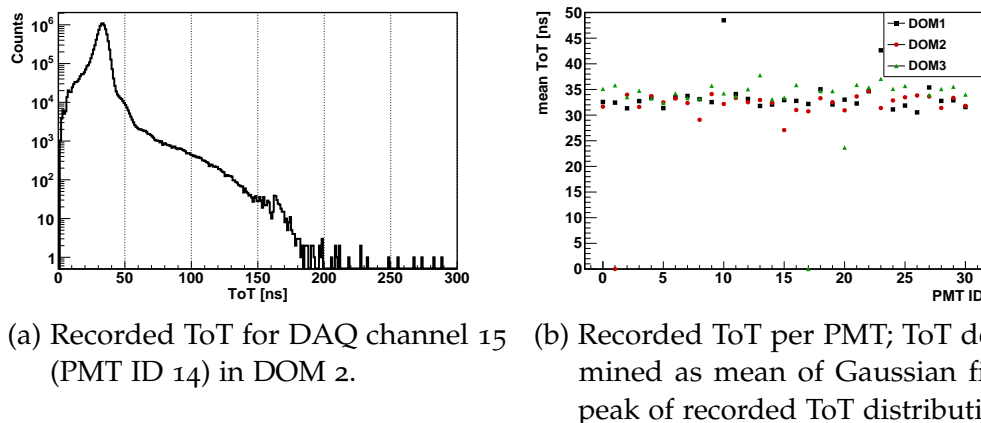
The procedure is limited by statistics in the ΔT histograms. It was found to perform with sub nano second precision for data period lengths down to 5 h.

The muon calibration was cross checked with the beacon calibration for data taken in phase 1. For data taking periods of sufficient length the two calibration procedures are found to be within 2 ns agreement.

4.5.7 Data period calibration

Calibration for the three different data taking periods of the PPM-DU varies because of the availability of nano beacon runs. In phase 1 runs with the nano beacon in DOM 1 flashing have been taken throughout it's duration and it can therefore be calibrated with the beacon method.

In phase 2 and 3 no beacon runs have been recorded. Due to the shifts in time offsets as discussed in Sec. 4.5.3 the time calibration is performed as follows. The time offsets estimated in phase 1 from the beacons are used as a basis for the muon time calibration. The data taking periods are subdivided into phases of data taking uninterrupted by a power cycle in the on- or off-shore hardware system. Each subperiod is then fitted with the muon calibration procedure to obtain the relative shifts from the phase 1 time offset shown in Tab. ??.



(a) Recorded ToT for DAQ channel 15 (PMT ID 14) in DOM 2. (b) Recorded ToT per PMT; ToT determined as mean of Gaussian fit to peak of recorded ToT distribution.

Figure 39: ToT study plots for run 311.

4.6 PPM-DU DATA ANALYSIS

4.6.1 Time over threshold signal

The time over threshold (ToT) as discussed in Sec. 4.3 is a quantity extracted from the analog PMT signal at the PMT base.

The ToT of a signal does not allow for an exact reconstruction of the number of incident photons. Two incident photons at the same time cause for instance a larger ToT than a single photon due to the larger amplitude of the resulting analog signal which roughly corresponds to 40 ns compared to the 30 ns for one photon [110]. But a second photo electron arriving during the falling flank of the first can cause a ToT of up to 60 ns.

A plot of the recorded ToT for a single PMT is shown in Fig. 39a. The distribution peaks around 30 ns since most of the recorded light is caused by single photo electrons created by potassium decays. The ToT is determined as the mean of a Gaussian fit to in a range of ± 4 ns around the mean of the ToT distribution. The resulting ToT for all PMTs in run 311 is shown in Fig. 39b. Most PMTs show a ToT around 33 ns, with the two turned off PMTs having no signals and therefore no recorded ToT. During the data taking the ToT was monitored by looking at the mean of the ToT distribution per PMT which yields an average ToT of 30 ns per PMT and therefore no HV retuning was performed. Two channels in DOM 1 show a significantly higher ToT and were re-tuned accordingly in later data taking.

4.6.2 Single rates

The single counting rate is the most rudimentary detector measurement and gives insight into the functionality of the PMTs. On each DOM a group of six PMTs share a high rate veto criteria. The veto is triggered when the six PMTs have an accumulated joined counting rate greater than 250 kHz in a time slice. Data is written until the count rate surpasses the veto value, once the veto value

is exceeded no more data is written for these PMTs. Due to the grouping of 6 PMTs per high rate veto one channel per DOM is left with a single high rate veto, DAQ channel 15. Hence the rate studies are performed with channel 15 to avoid high rate veto influence.

Two PMTs out of the 93 have been found faulty and are not used. DAQ channel 27 (PMT ID 17) in DOM 3 was found to saturate the high rate veto continuously and was therefore turned off. DAQ channel 14 (PMT ID 1) in DOM 2 was not reachable after DOM assembly. The remaining 91 PMTs are fully operational.

For triggered data files the singles rate per slice is stored in the so-called summary slices data structure. The recorded rates for one PMT and run are shown in Fig. 40a. The rate is stored in a 8 bit compressed datum with a higher resolution in the region of interest from 5.5 kHz to 7.5 kHz. The rate shows a Gaussian distribution around the mean of 6.5 kHz with a tail towards higher values. These two parts of the distribution correspond to different physical sources. The Gaussian distribution is caused by potassium decays and PMT dark rate while the tail is caused by bursting bioluminescence events.

In order to check the data recorded in the summary slices a second method was used to determine the singles rates. For this purpose untriggered data files are used. By recording the time difference of consecutive hits on the same PMT the single rate can be determined. A histogram of such a distribution for DAQ channel 15 (PMT ID 14) in DOM 2 for run 311 is shown in Fig. 40b. The histogram shows structure around at time differences around 3 μ s. At late time differences an exponential decay of the single rate is observed. The structure around 3 μ s is caused by so called afterpulses in the PMTs. These originate due to rest gas atoms inside the PMT vacuum tube which can be ionized and due to their higher mass arrive later. The time difference is typical for the expected rest gas ions from PMT production. By fitting the exponential decay part the single rate of each PMT can be obtained. The used fit function is

$$f(x) = p_0 \times \exp(-p_1 \times x) \quad ,$$

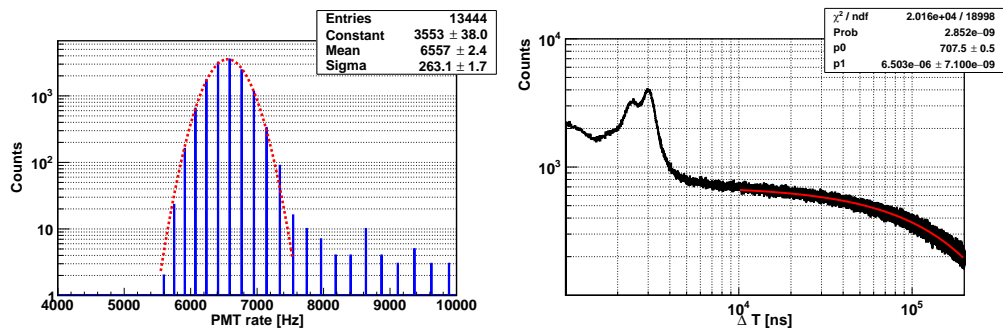
where p_1 is the rate and p_0 is a scaling factor.

Comparing both methods the results are found to be summary 6557 Hz and exponential 6503 Hz which agree reasonably well. The resulting rates from the exponential fits for run 311 are shown in Fig. 40c. The PMTs in DOM3 show a systematically higher rate, this is caused by the higher PMT efficiency as discussed in Sec. 4.2.

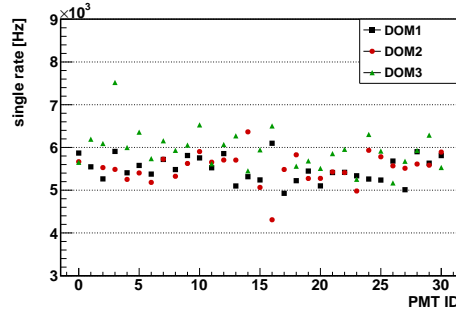
The counting rate of the PMTs are well understood. Two different methods are established to monitor them which are in good agreement. This knowledge of the single rates is needed as input to the background simulations and the time calibration as discussed previously.

4.6.3 Recorded triggered events

The trigger algorithms are discussed in Sec. 4.3.1. A comparison of the trigger rates between data and MC helps to identify trigger settings which separate



(a) Rate per summary slice for DAQ channel 15 (PMT ID 17) in DOM 2; red line shows Gaussian fit. (b) Consecutive hits on same PMT for DAQ channel 15 in DOM 2; red line shows exponential fit.



(c) Obtained single rates from exponential fit.

Figure 40: Single rate study plots for run 311.

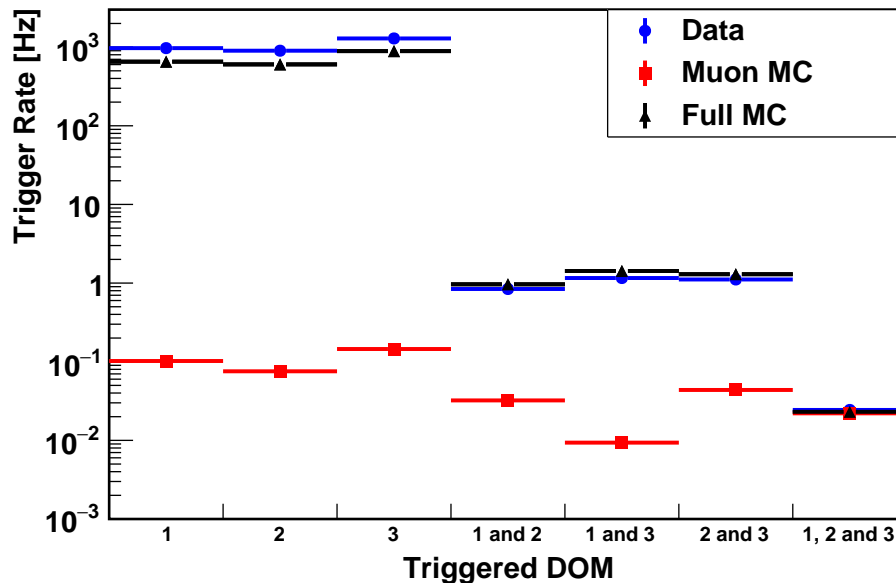


Figure 41: Rate of the different triggered events by DOMs with at least one L1 hit of all triggered events in phase 2, Full MC is the muon MC plus potassium MC.

muon and background events. Shown in Fig. 41 are the rates of the different types of triggered events. The triggered events either have a single DOM, two DOMs or three DOMs with L1 hits within the trigger time window. The different number of DOM triggers are plotted in an exclusive manner. For example a 3 DOM trigger event is not counted as a 2 DOM trigger events as well. As can be seen the single DOM and two DOM triggered events are dominated by random potassium background, while the three DOM triggers are dominated by muon signals. The over estimation of the data in the MC for single DOM triggers of around 30 % and the underestimation of 2 DOM triggers of around 30 % is significant and points to a flaw in the corresponding calculations of the expected random coincidences by potassium decays (see Sec. 4.4).

4.6.4 Muon detection

The detection of muon signals with the PPM-DU illustrates the advantages of multiple PMTs in the same DOM. Already a single multi-PMT DOM allows a discrimination between potassium and muon signals.

A method to distinguish random background and physical events is made possible by observing correlated signals in different PMTs on a DOM. A plot of the recorded coincidences in phase 2 is shown in Fig. 42a. The distribution in data and full MC (muon and potassium MC added together) both show two regimes of different slope. The larger slope from coincidence size 2 to 6 is dominated by coincidences from potassium decays. The higher rate of DOM 3 in this area is caused by the higher total detection efficiency of the Hamamatsu PMTs. The region of with a smaller slope from coincidence size 7 and upwards

matches that of the muon data shown in the filled histograms. Coincidences of size 7 and greater are therefore dominated by muon events.

A plot of the ratios between data and MC is shown in Fig. 42b. The data and MC show good agreement for coincidences of size three while deviating for size two and in the region of coincidence size 4 to 6. For these coincidence sizes the MC underestimates the MC and for coincidence sizes 4 to 6 the underestimation gets more drastic with increasing coincidence size. This deviation is caused by two different effects, namely: The simulation of random coincidences and the PMT efficiency.

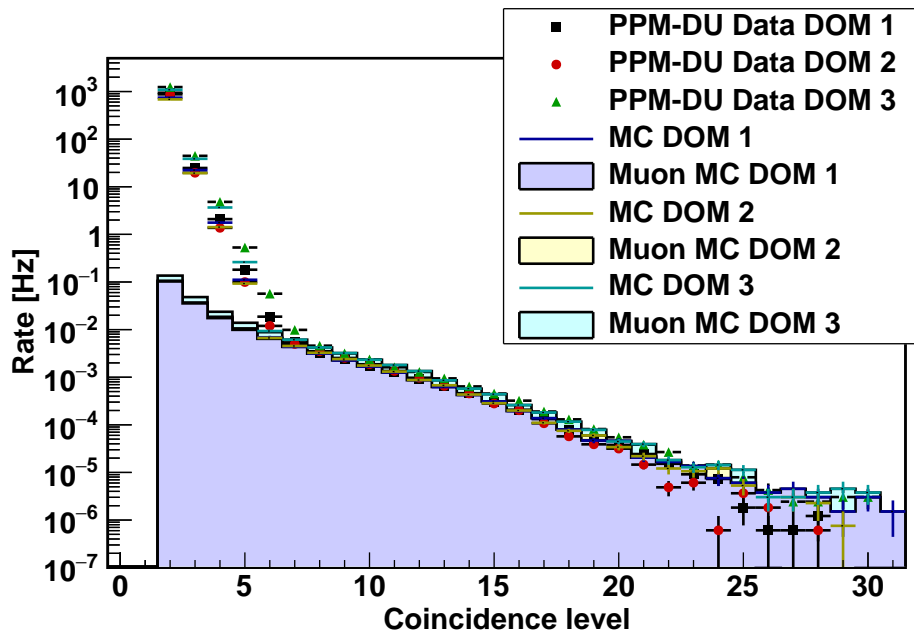
For coincidence size two the dominant contribution is due to random coincidences and spurious pulses may have a significant influence. These effects are not taken into account in the simulation. Therefore, the data is underestimated, especially for the two ETEL DOMs. For coincidence sizes larger than two the random background contribution is negligible causing the MC to match the data well for coincidences of size three. With increasing coincidence size the deviation of the MC starts to grow exponentially. This effect is most likely caused by an underestimation of the efficiencies which indeed affects the rate exponentially with increasing coincidence size. This effect is most likely caused by the angular acceptance of the PMTs on potassium decays. The larger the coincidence the more likely it is to observe light at large incident angles on the PMT cathode. The MC simulation therefore seems to underestimate the angular acceptance of the PMTs, causing the agreement between data and MC to worsen in that regime. From coincidence 7 to 18 data and MC are in good agreement. At coincidence sizes 19 and upward MC starts to overestimate the number of events. The cause for this is not identified yet but could be correlated with the assumed water parameters. The difference in data between DOM 1 and the other two at the largest coincidence sizes is caused by the fact that only DOM 1 has 31 PMTs operating. Therefore DOM 1 has a higher chance of detecting large coincidences and is the only DOM that can record coincidences of size 31. The illumination of a DOM is not strongly correlated with the energy of the muons but rather with the distance between the muon and the DOM. Coincidence sizes of 25 and larger are mainly caused by muons which are within 10 m distance of closest approach to the PPM-DU.

In order to confirm the observation that coincidences of size 6 and larger are muon events the zenith pattern of the hit PMTs gives further insight. For an atmospheric muon to reach the detector it has to traverse about 3.5 km sea water. Due to the energy loss most muons are down-going (zenith angle close to 0°). The expected angular distribution of the atmospheric muons would cause a characteristic signature in the multi-PMT DOMs. Since PMTs which point towards the muon track have a higher possibility to be hit by Cherenkov light, it is expected that the upward looking PMT rings E and F to record more hits than the downward looking PMT rings.

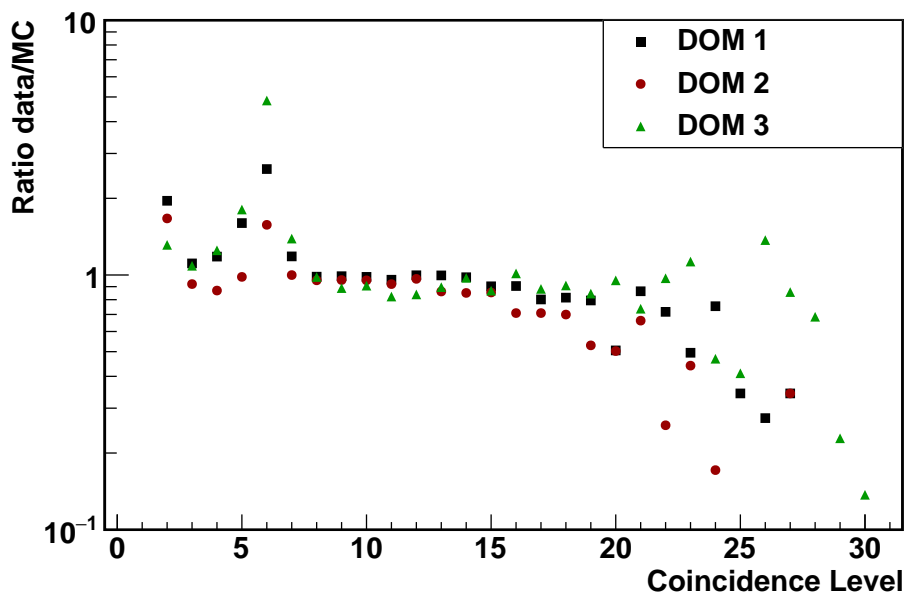
A histogram of the hit PMTs for coincidence sizes 6 and greater is shown in Fig. 43. As can be seen, all three DOMs show significantly more hits in the upward pointing rings. This confirms the conclusion drawn from Fig. 42a that coincidence of sizes 6 and larger are dominated by muon events. Comparing

the data and MC in this plot shows a difference in the expected rates in the individual PMTs although the MC is adjusted with the estimated efficiencies. This could be caused by the fact that the efficiencies are estimated using potassium decays. The light observed by the PMTs for muon events is mainly produced via the Cherenkov effect. The PMT efficiencies for these two light sources could be different. For instance the wavelengths or the angle of the incident photons could be different, causing the effective efficiencies to vary. The difference in the overall scale per DOM is caused by the fact that DOM 3 and 2 are more likely to be hit by muon light than DOM 1 since they are higher up and therefore more muons can reach them and the higher efficiency of PMTs in DOM3.

For a muon event the light arrival time on the DOMs is correlated with the travel time of the muon along the string. The travel time of the muons depends on the zenith angle of the muons, with straight down-going muons having the shortest travel time. The energy of a muon does not affect the travel time since at the typical energies of 1 GeV or higher all muons travel at the speed of light. For the purposes of studying the muon travel time the time difference between the first L1 hits on each DOM are an ideal measurement. The histograms of DOM time differences for two and three triggered DOM events are shown in Fig. 44. Both histograms show a distinct peak in the distribution that corresponds to muons traveling down along the PPM-DU. The shapes of the peaks are correlated with the zenith distribution of the muons, the detection efficiency of the PMTs and the scattering length of light in water. The two DOM trigger histogram shows the peak above a constant background of random coincidences while the three DOM histogram is almost background free. The difference in random background between different DOM triggers was already shown and discussed in Sec. 4.6.3. The shapes of the data is reproduced by the MC scaled by entries showing that the simulated muon fluxes per angle is in good agreement with what is measured in the deep sea. For difference scaled by lifetime see the corresponding entries shown in Fig. 41.



(a) Rate as function of size of recorded coincidences in phase 2 data taking period; Filled histograms show the muon MC, lines without markers muon and potassium MC added and lines with markers the data; MC scaled by lifetime to the data.



(b) Ratio between lifetime scaled data and MC for different recorded coincidence sizes as shown in Fig. 42a in phase 2 data taking period.

Figure 42: Coincidence size studies for phase 2 data taking.

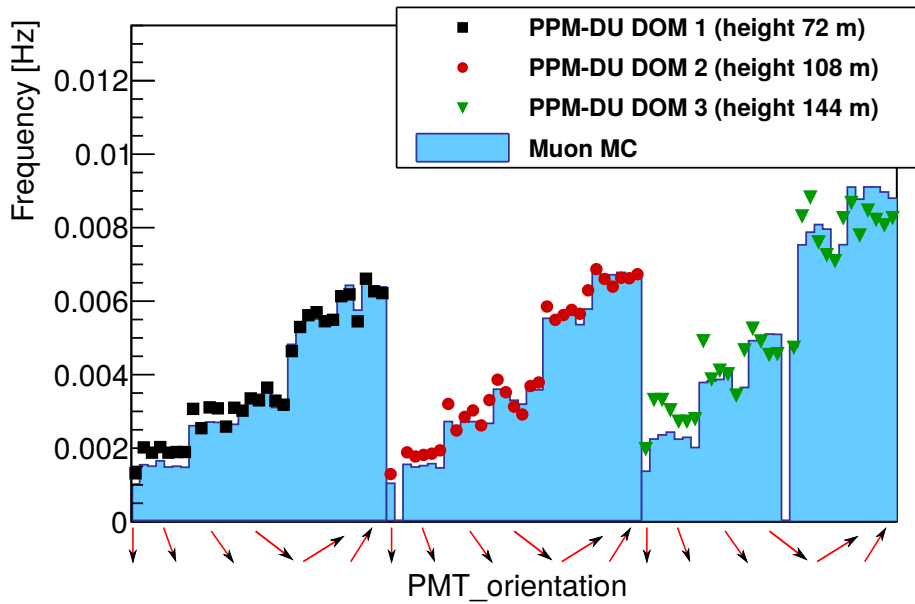
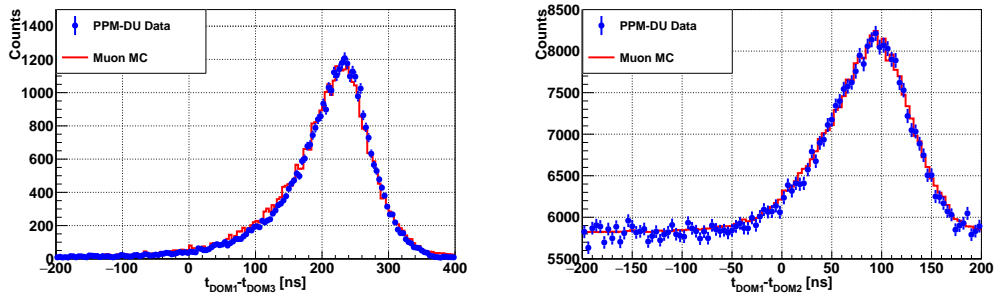


Figure 43: Rate of PMTs for events of coincidence size 6 and greater; Filled histograms show the muon MC, markers the data; MC scaled by lifetime to the data per DOM.



(a) Time difference between first L1 on DOM 1 and DOM 3 in case of a three DOM trigger (at least one L1 on each DOM).

(b) Time difference between first L1 on DOM 2 and DOM 3 in case of a two DOM trigger (at least one L1 on DOM 2 and 3, no L1 on DOM 1).

Figure 44: DOM ΔT distributions for the first L1 on each DOM; event selection is exclusive (no double counting of three DOM triggers); MC scaled to data by entries.

4.7 MUON RECONSTRUCTION

The reconstruction of the muon tracks with the PPM-DU is a first step towards the analysis needed for a fully operational KM₃NeT detector. The final goal of a neutrino telescope is the detection and reconstruction of neutrino events. For the reconstruction of neutrino events two different channels have to be distinguished, the shower and the track events. Of these two types the track reconstruction is attempted with the available number of DOMs.

A charged particle traveling through the water at the speed of light continuously radiates Cherenkov photons in a characteristic angle of about 42°. This so called Cherenkov cone allows for a reconstruction of a straight trajectory due to a muon passing by the PPM-DU.

The track reconstruction algorithm used is based on the Antares single line fit [111]. A track can be parameterized as a function of arrival time of the Cherenkov photons on the DOMs as given by

$$t = \left[(z - z_0) * \cos \theta + \sqrt{n^2 - 1} * \sqrt{d_0^2 + (z - z_0)^2 * (\sin^2 \theta)} \right] / c + t_0 \quad , \quad (19)$$

where t_0 , z_0 , d_0 are the time, height and distance of the point of closest approach between DOM and track, n is the refractive index of light in water, θ is the zenith angle of the track and t is the expected hit time on the DOM. An example sketch of a muon event and the parameters are shown in Fig. 45.

In order to select a clean muon sample only events with three triggered DOMs are considered. As discussed in Sec. 4.6.3 this selects an almost background free muon sample.

This single line track fit suffers from symmetric solutions in the ϕ angle of the track. These are caused by the fact that a single string without taking into account the position of the hit PMTs can not distinguish between rotation symmetric solutions around the z -axis. The fact that the PPM-DU only includes three DOMs introduces further degeneracies in the track fit. A track that neglects the ϕ reconstruction as shown in Eq. 19 has four degrees of freedom. Therefore by using one hit time per DOM degeneracies in the solution phase space are caused. By a proper selection of the phase space these degeneracies can be reduced.

4.7.1 Fitting procedure

All events with three triggered DOMs are processed in the reconstruction. From the triggered hits the start values of the fit are deducted. The mean z height (z_{mean}) and mean time (t_{mean}) of all hits that compose a L1 hit on the three DOMs is calculated. The starting values of the fit are then set as $t_0 = t_{\text{mean}}$, $z_0 = z_{\text{mean}}$, $d_0 = 0$ and $\cos \theta$ is varied between 1 to 0.505 in steps of 0.005. For every value of $\cos \theta$ Eq. 19 is minimized using the ROOT Migrad

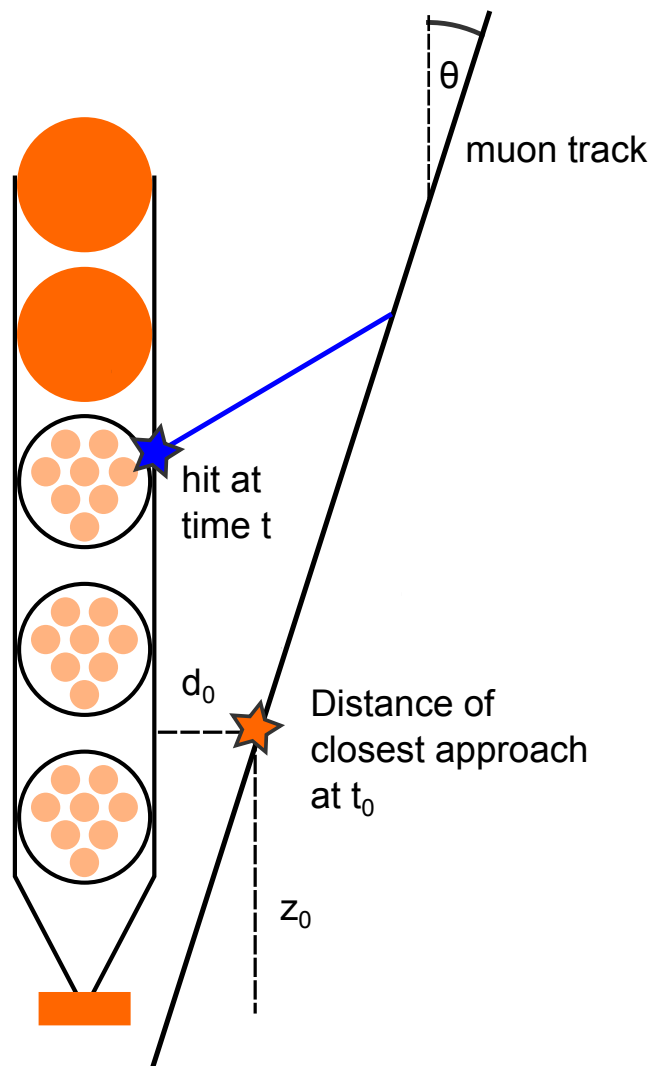


Figure 45: Sketch of a muon event passing the PPM-DU with the parameters of a parametrization discussed in Eq. 19.

minimizer [101]. The χ^2 of each fit is calculated based on the hit time residuals of all triggered hits to the fitted track as shown in Eq. 20

$$\chi^2 = \sum_i \left(t_{\text{hit}}^i - \text{expected } t_{\text{hit}}^i \right)^2, \quad (20)$$

where t_{hit}^i is the hit time of all Lo hits composing the L1 hits and the expected hit time is based on the reconstructed track. The best fit is selected as the fit with the lowest χ^2 . Every reconstructed event is then discriminated based on selection criteria discussed in Sec. 4.7.2.

4.7.2 Event selection

The event selection is an essential part of the reconstruction in order to limit the influence of the degeneracies in the solution phase space. A way to identify regions with degeneracies is by calculating the expected DOM time differences from Eq. 19 for a set of values. Therefore the parameters of Eq. 19 are varied as follows: $\cos \theta$ from 0.98 to 0.5 in different step sizes (see legend of Fig. 46a), d_0 from 0 m to 10 m in steps of 1 m and z_0 from $\text{DOM}_1.z - 30$ m to $\text{DOM}_3.z + 30$ m in steps of 1 m. The resulting DOM time differences are shown in Fig. 46a. The different solutions show specific characteristics that can be exploited to select regions with minimum degeneracies and reject unphysical events. The regions with most overlays in different $\cos \theta$ distributions are at $t_{\text{DOM}_1} - t_{\text{DOM}_2} \geq 150$ ns ($\Delta T_{12} \geq 150$ ns) and tracks approaching horizontal directions. Since tracks that approach horizontal directions are suppressed naturally by the small amount of muons reaching the detector at these angles the corresponding regions is not excluded by a specific selection. Three other selections on the DOM time differences have been performed in order further limit the selection of tracks with reasonable phase space: -50 ns $\leq \Delta T_{12} \leq 150$ ns, -50 ns $\leq \Delta T_{23} \leq 165$ ns and $\Delta T_{23} - \Delta T_{12} \leq 10$ ns. The selections on the DOM time differences cuts out a triangle as indicated by the black lines shown in Fig. 46a.

The distribution of data events in the DOM time differences is shown in Fig. 46b together with the selections. As can be seen a low amount of the events lies outside of the selection. These are mainly events caused from random coincidences. The main part of the data is in the region of down-ward going muons which we expect from the survival probability of the muons. The area at ΔT_{12} between 150 ns to 160 ns shows a significant number of events and is excluded, but since the highest degeneracies are expected in this region no well reconstructed tracks are lost

A selection on the distance of closest approach between the PPM-DU and the muon track was performed. The effect of the distance on the degeneracies is shown in Fig. 47, here the variables are the same as shown in Fig. 46a except for d_0 was varied from 10 m to 20 m (instead of 0 m to 10 m). The tracks with larger distances cause high degeneracies, even at highly down-ward going angles. The distance of closest approach was therefore selected to be $d_0 \leq 10$ m.

The rate of selected events for the selection criteria in data and MC are shown in Fig. 48. The rates are inclusive and the selection criteria are applied from

left to right as shown in the figure. An event that is rejected by one criterion is therefore not passed on to the next. It can be seen that the MC is underestimating the data by roughly 10%. This factor is observed in all comparisons. Except for the offset the MC and data match nicely for all selection criteria. We can also observe that after cutting on $d_0 \leq 10$ m the last cut on unphysical events $\Delta T_{23} - \Delta T_{12} \leq 10$ ns rejects no further events, proving the distance of closest approach cut to be effective in rejecting unphysical events.

The performance of the cuts on the reconstructed zenith angle resolution is shown in Fig. 49. Although well reconstructed events are lost during the selection, the tails towards badly reconstructed events are highly suppressed. This shows that the sample of select tracks is of high quality.

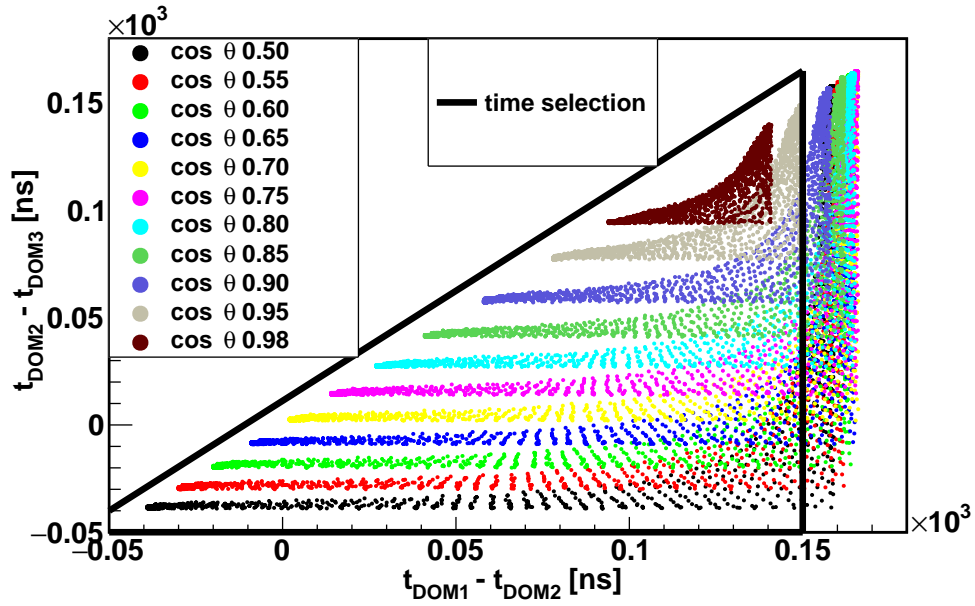
4.7.3 Zenith angle reconstruction

The goal of the track reconstruction is the identification of muons passing the PPM-DU. Since the Φ angle is neglected, the zenith angle θ is the only parameter that can be sensibly reconstructed. The distance of closest approach between line and track is needed for the track reconstruction, but the parameter itself holds little physical interest.

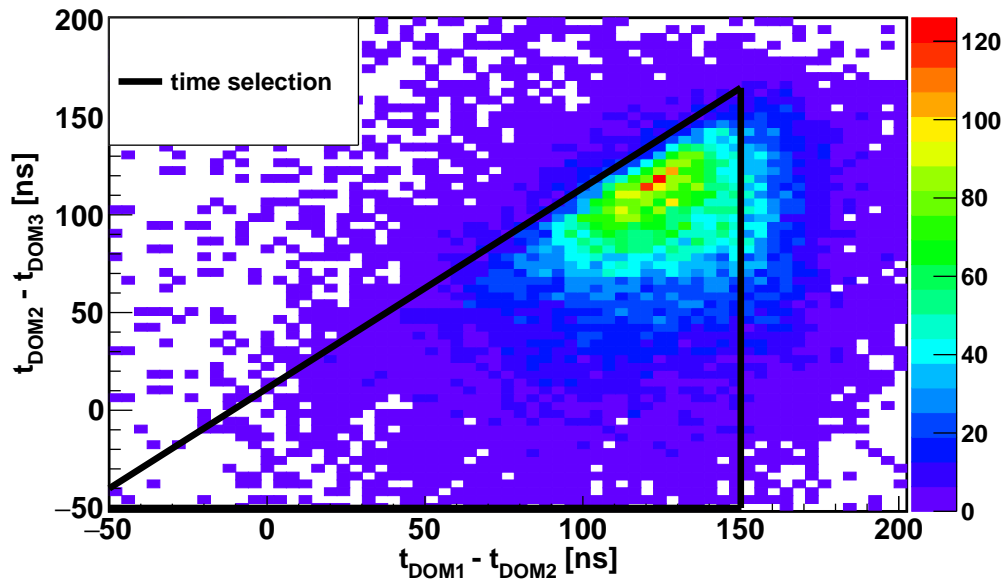
The θ angle is of high interest for MC studies. It can probe if the production of the muons in the atmosphere and the propagation through the sea water is performed correctly.

The resolution of the zenith angle reconstruction is determined using the MC production. By comparing event by event the reconstructed angle with the simulated angle the resolution can be determined. In Fig. 49 the resulting resolution is shown. The reconstruction after selection criteria achieves in angular resolution of 8.3° RMS.

The reconstructed $\cos\theta$ distribution is shown in Fig. 50. As discussed previously the MC underestimates the data by roughly 10%. Except for that offset, data and MC are in excellent agreement.



(a) Possible DOM time differences for Eq. 19 and different $\cos \theta$; varying d_0 from 0 m to 10 m in steps of 1 m and z_0 from 30 m below DOM_1 to 30 m above DOM_3 in steps of 1 m.



(b) DOM time differences of all three DOM trigger events in phase 2.

Figure 46: Solution phase space studies in DOM time difference distributions; the black lines indicate the performed selection for DOM time differences.

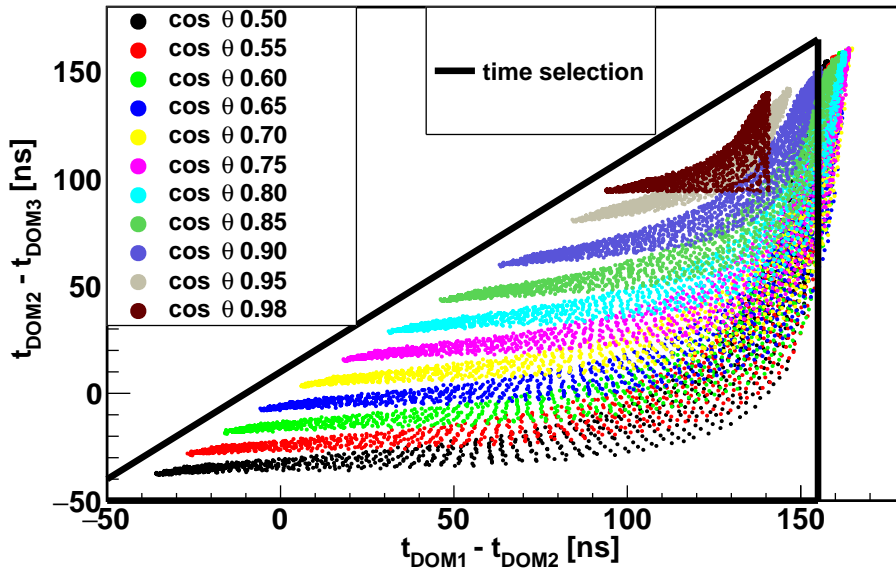


Figure 47: Possible DOM time differences for Eq. 19 and different $\cos \theta$; varying d_0 from 10 m to 20 m in steps of 1 m and z_0 from 30 m below DOM_1 to 30 m above DOM_3 in steps of 1 m.

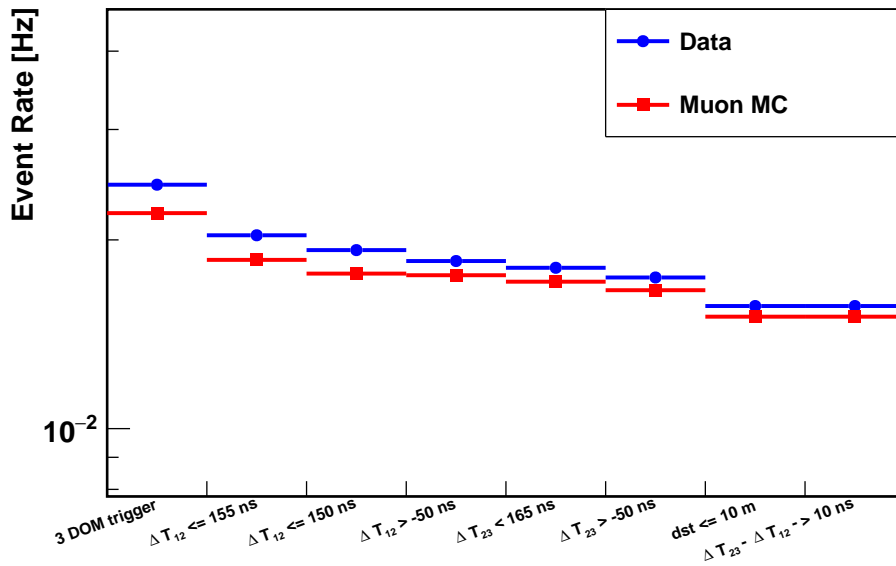


Figure 48: Event rate of all performed selection criteria of the muon reconstruction; event rates are inclusive and selections are performed from left to right.

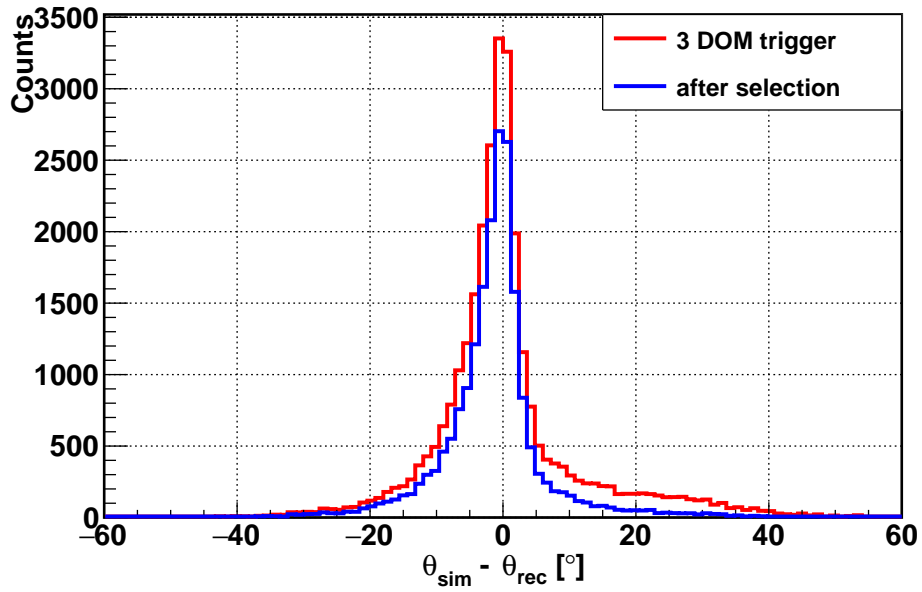


Figure 49: Zenith resolution of the reconstructed tracks for all three DOM trigger events and events that pass the selection respectively.

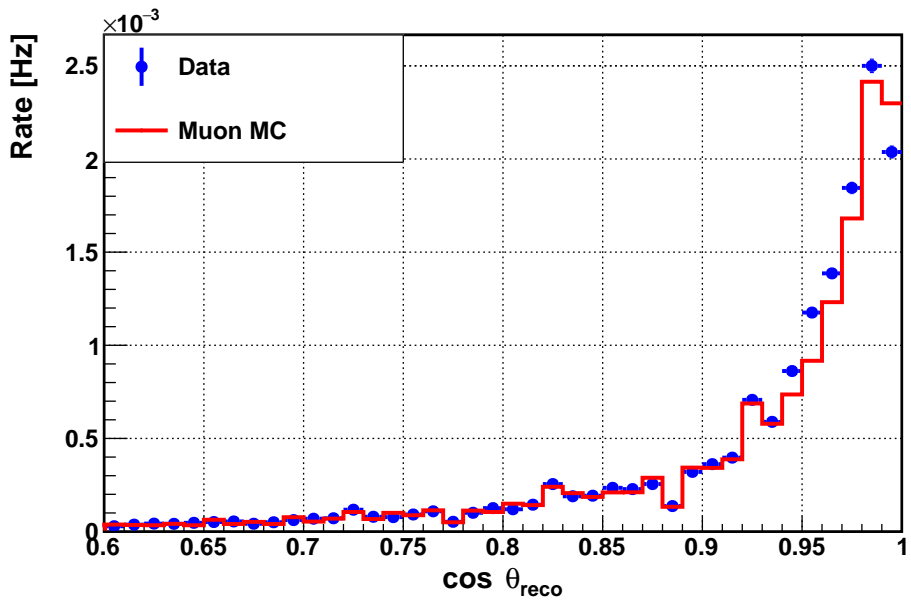


Figure 50: Reconstructed cosine of the zenith angle in data and MC.

4.8 PPM-DU CONCLUSION

The deployment of the string prototype proved a great success for the KM₃NeT collaboration. Especially regarding the calibration procedures and technical design.

The successful deployment and installation of the prototype was the first of a string with operational DOMs proving the procedures to be working. The use of different PMTs allowed for a direct in-situ comparison showing the advantages of the Hamamatsu PMTs.

The in-situ calibration of the PMTs utilizing the light from potassium decays proved to be working, thereby laying the ground for the in-situ PMT calibration of future detection units.

The time calibration between DOMs using the atmospheric muons and/or the LEDs showed to be working but needs further improvement in the future in order to achieve the 1 ns timing accuracy needed for the KM₃NeT detector.

The studies of the basic detector operations such as single rates and ToTs proved the basic understanding of the detection unit. Building on that and the results from the previous DOM prototype the identification of the atmospheric muons was performed utilizing the multi-PMT design.

The follow up muon reconstruction was based on a basic algorithm. Therefore, only a zenith angle reconstruction was possible. Different approaches utilizing the multi-PMT design in order to achieve azimuth sensitivity were performed but did not lead to a firm conclusion.

In total, the string prototype laid many important ground work for the first full strings to build upon. Allowing to prepare detector operation and data analysis for the KM₃NeT detector.